Magnetic resonance imaging of human knee joint functionality under variable compressive *in-situ* loading and axis alignment

Philipp Schad [a], Maximilian Wollenweber [a], Johannes Thüring [a], Justus Schock [b,c], Jörg Eschweiler [d], Giulia Palm [e], Klaus Radermacher [e], Felix Eckstein [f,g,h], Andreas Prescher [i], Christiane Kuhl [a], Daniel Truhn [a,c], Sven Nebelung [b,*]

[a] *Department of Diagnostic and Interventional Radiology, Aachen University Hospital, Aachen, Germany*
[b] *Institute of Diagnostic and Interventional Radiology, University Hospital Düsseldorf, Düsseldorf, Germany*
[c] *Institute of Computer Vision and Imaging, RWTH Aachen University, Aachen, Germany*
[d] *Department of Orthopaedic Surgery, Aachen University Hospital, Aachen, Germany*
[e] *Helmholtz-Institute for Biomedical Engineering, Chair of Medical Engineering, RWTH Aachen University, Aachen, Germany*
[f] *Department of Imaging & Functional Musculoskeletal Research, Institute of Anatomy & Cell Biology, Paracelsus Medical University Salzburg & Nuremberg, Salzburg, Austria*
[g] *Chondrometrics GmbH, Ainring, Germany*
[h] *Ludwig Boltzmann Institute for Arthritis and Rehabilitation, Paracelsus Medical University, Salzburg, Austria*
[i] *Institute of Molecular and Cellular Anatomy, RWTH Aachen University, Aachen, Germany*

ARTICLE INFO

ABSTRACT

Magnetic resonance imaging (MRI) under mechanical loading, commonly referred to as stress MRI, allows the evaluation of functional properties of intra- and periarticular tissues non-invasively beyond static assessment. Quantitative MRI can identify physiological and pathological responses to loading as indication of, potentially treatable, early degeneration and load transmission failure. Therefore, we have developed and validated an MRI-compatible pressure-controlled axial loading device to compress human knee specimens under variable loading intensity and axis deviation. Ten structurally intact human knee specimens (mean age 83.2 years) were studied on a 3.0T scanner (Achieva, Philips). Proton density-weighted fat-saturated turbo spin-echo and high-resolution 3D water selective 3D gradient-echo MRI scans were acquired sequentially at 10° joint flexion in seven configurations: unloaded and then at approximately half and full body weight loading in neutral, 10° varus and 10° valgus alignment, respectively. Following manual segmentation in both femorotibial compartments, cartilage thickness (ThC) was determined as well as meniscus extrusion (ExM). These measures were compared to computed tomography scans, histological grading (Mankin and Pauli scores), and biomechanical properties (Instantaneous Young's Modulus).

Compartmental, regional and subregional changes in ThC and ExM were reflective of loading intensity and joint alignment, with the greatest changes observed in the medial compartment during varus and in the lateral compartment during valgus loading. These were not significantly associated with the histological tissue status or biomechanical properties.

In conclusion, this study explores the physiological *in-situ* response of knee cartilage and meniscus, based on stress MRI, and as a function of loading intensity, joint alignment, histological tissue status, and biomechanical properties, as another step towards clinical implementation.

1. Introduction

Due to its non-invasiveness, superior soft tissue contrast, high spatial resolution, functional capability, and absence of ionizing radiation, magnetic resonance imaging (MRI) is considered the most powerful and versatile imaging modality in contemporary clinical medicine. While MRI undisputedly constitutes the reference standard in the diagnostic work-up of numerous musculoskeletal conditions and joint pathologies, clinical standard MRI techniques have some deficits in the diagnosis of

Abbreviations

ax	axial
BW	body weight
cLF	central lateral femur
cMF	central medial femur
cor	coronal
CT	computed tomography
ExM	meniscus extrusion
fs	fat-saturated
IYM	Instantaneous Young's Modulus
LM	Lateral Meniscus
LT	lateral tibia
MM	Medial Meniscus
MRI	Magnetic Resonance Imaging
MT	medial tibia
OA	osteoarthritis
PA –	polyamide
PDw	proton density-weighted
PVC	polyvinyl-chloride
sag	sagittal
SPAIR	spectral attenuated inversion recovery
ThC	cartilage thickness
WATSc	water selective cartilage scan

intra- and periarticular knee joint pathologies (Jandaghi et al., 2016; Palmer et al., 2013; Phelan et al., 2016). In clinical MRI studies, patients are routinely imaged supine, with the knee unloaded, unlike the relevant physiological condition. Unloading fundamentally alters the knee joint's morphological configuration and functional status, which has strengthened efforts aimed at examination conditions that are more reflective of the knee joint's physiological configuration during load bearing and motion (Jerban et al., 2020; Patel et al., 2016; Souza et al., 2010, 2014).

Degenerative structural and compositional changes in osteoarthritis (OA) significantly alter the tissues' mechanical properties (Fischenich et al., 2015; Kleemann et al., 2005; Saarakkala et al., 2010). Biomechanical imaging techniques may thus be applied to quantify such changes based on MRI measures as surrogate parameters of tissue functionality (Eckstein et al., 2005; Herberhold et al., 1999; Nebelung et al., 2017b, 2020; Truhn et al., 2019). Loading-induced changes in the morphological features of cartilage and meniscus, i.e. volume, thickness, contact area, and position, have been investigated *in vivo*, differentiating OA from non-OA knees (as reviewed by (Jerban et al., 2020)). Based on such stress MRI techniques, aberrant tissue functionality has been determined, with OA knees undergoing greater reductions in cartilage thickness (Cotofana et al., 2011), greater deformations (Subburaj et al., 2012), and greater increases in femorotibial contact areas (Shin et al., 2011) and in meniscus extrusion (Patel et al., 2016) than healthy, structurally normal knees. Although these studies have focussed on the diagnostic potential of stress MRI, the loading conditions were generally not well defined and standardized. Moreover, these clinical studies used the radiographic Kellgren-Lawrence classification (Kellgren and Lawrence, 1957) for patient stratification and allocation, which is a highly disputed reference (Roemer et al., 2011, 2018). Likewise, these clinical studies did not obtain detailed information on the cartilage and meniscus status to be related to the response-to-loading patterns. Knowledge of joint and tissue functionality across a wide range of physiological and pathological conditions is thus still scarce.

This study was therefore designed to develop and validate an MRI-compatible pressure-controlled axial compressive loading device and to compress human knee specimens under variable loading intensity and axis deviation in a standardized and controlled experimental *in-situ* setting. Joint functionality was explored in relation to computed tomography (CT) as well as histological and biomechanical measures of cartilage and meniscus. We tested the following hypotheses: 1, human knee joints undergo consistent changes in imaging biomarkers when loaded by means of a dedicated axial compressive loading device; 2, the response to loading as assessed by high-resolution morphological MRI differs between knee compartments as a function of loading intensity and mechanical axis alignment; 3, these response-to-loading patterns are related to histological and biomechanical properties of cartilage and meniscus.

2. Materials and methods

2.1. Study design

This study was conducted in two phases: 1, development and validation of an MRI-compatible pressure-controlled axial compressive loading device; and 2, systematic study of intraarticular changes in human knee specimens based on MRI (and CT) and as a function of variable biomechanical loading conditions.

2.2. Axial compressive loading device

2.2.1. System design

The MRI-compatible pressure-controlled axial compressive loading device was designed for compressive loading of single human knee joint specimens in a constrained manner and in various experimental settings, i.e. variable joint flexion angles (0°–20°) and joint alignment (axis deviations; 0°–10° varus - 10° valgus). The device consists of an MRI-compatible loading unit within the scanner, and of a separate control unit for remote control outside the scanner. Below, *mechanical axis* refers to the knee joint's *anatomical axis*, as no additional information on the remaining lower extremity's overall anatomy or biomechanics were available for the individual knee joint specimens. For details, please see 2.3 Human Knee Joint Specimens below.

2.2.2. Loading unit

The loading unit (displayed in detail in Fig. 1) was made of synthetic MRI-compatible materials, i.e. polyamide (PA), polyvinyl-chloride (PVC), and ABS-M30, a 3D-printable thermoplastic (Stratasys Inc., Eden Prairie, MN, USA). Any mechanical fasteners such as screws, bolts, and rods were made of PA, while the restoring spring and all remaining components were made of ABS-M30 and PVC, respectively.

The solid base plate was dimensioned to take any bending moments and counter forces during loading. Mounting blocks located on both sides of the joint were firmly attached to the base plate via PA screws. On the **tibial side**, the pneumatics was attached to and contained within the mounting block. The loading piston contained in the pneumatics was fed via standard pressure lines (PUN-6X1-BL, Festo, Esslingen, Germany) connected to the cylinder head's pressure port. The loading piston (radius $r = 3.25$ cm) was laid out to generate a (theoretical) maximum compressive force (F_{com}) of approximately twice body weight (BW) with maximum pressure levels of pressure $p_{max} = 4.69$ bar as provided by the in-hospital pressure outlets ($F_{com} = \pi * r^2 * p = 1556\ N$). Pressurization actuated the spring bolt, which in turn displaced the rigid fork mountings and, eventually, the tibia. For the perspective implementation of dynamic loading regimes, a restoring spring (material: ABS-M30; inner/outer diameter: 32/48 mm; length: 53.4 mm with pretension of 10 mm; spring constant: 4356 N/m, printed on a 3D rapid prototyping printer [Dimension SST 1200es, Stratasys]) was included in the pneumatics. The restoring spring surrounded the spring bolt to smoothly guide the
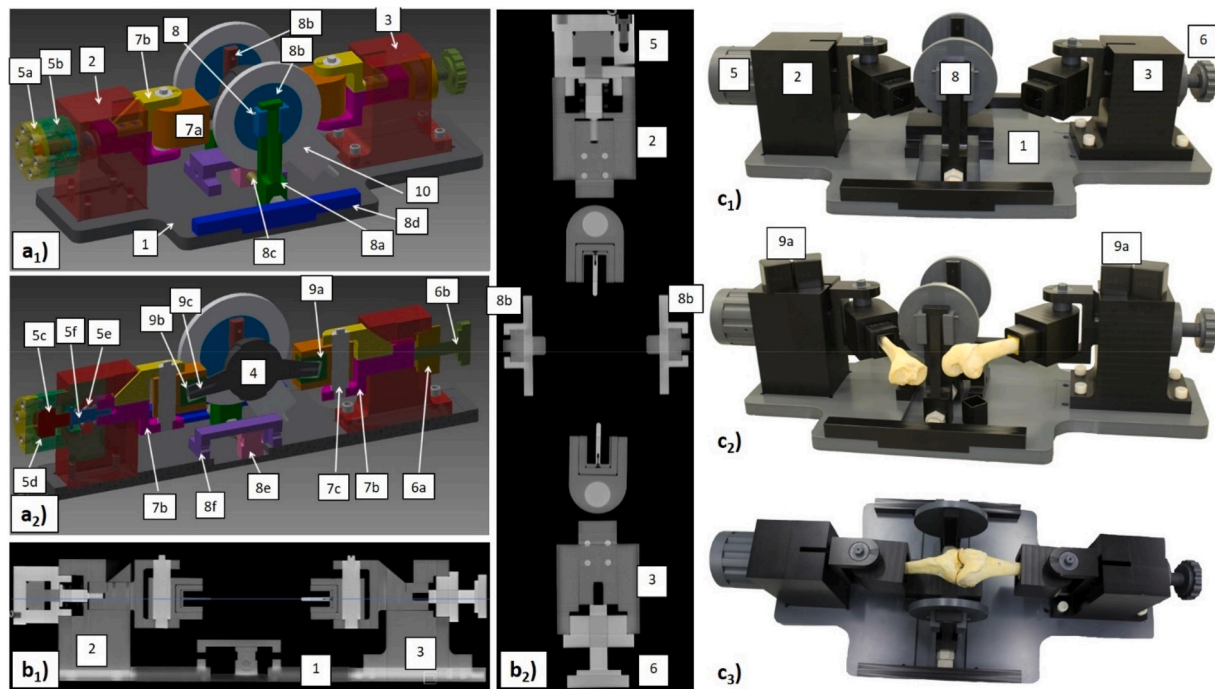
Fig. 1. CAD schemes (a), reconstructed CT views (b), and photographs (c) of the axial compressive loading device. a) Total view (a_1) and cross-sectional view (a_2). All components are firmly attached to the solid base plate (1). The mounting blocks on both sides of the joint provide pressure-controlled displacement of the tibial side (2) versus the rigidly fixed femoral side (3) of the human knee joint specimen (4). On the tibial side, the pneumatics consist of the cylinder head (5a) and pneumatic cylinder (5b), which contains the loading piston (5c), seal ring (5d), restoring spring (5e), and associated spring bolt (5f). On the femoral side, compensation of specimen length is realized by a threaded adapter component (6a) driven by an adjusting screw (6b). Principally, the joint may be set to variable varus and valgus deviations by rotatable holding blocks (7a) that are mounted on rigid fork mountings (7b) and allow for rotation along their studs (7c). Axis deviation is also secured by the varus-valgus positioning unit (8) consisting of two parallel abutments (8a) with fitted press-point discs (8b) that may be adjusted in the mediolateral plane along a threaded rod (8c) centered by firmly attached counter-bearings (8d). Analogously, different specimen lengths are compensated by an adjustable sliding block (8e) in a centering guide element (8f). Defined joint flexion angles may be set by appropriately angled bone adapters (9a) that contain the bone end pots (9b) and an additional spike (9c) for fixation purposes. The multi-purpose coils used for MR imaging (10) circumferentially comprise the press-point discs at the medial and lateral aspect of the joint. b) Sagittal (b_1) and axial (b_2) reconstructions of CT data (without specimen). The light blue line (in b_1) indicates the sectional plane of b_2. c) Device in the unloaded (c_1), loaded-nonoperational (c_2), and loaded-operational configurations (c_3). In c_2 and c_3, the device is loaded with a human femur and tibia for visualization purposes.

loading piston back to the starting position upon release of pressure. Upon pressurization, the tibial-sided rigid fork mountings were displaced towards the knee joint. Mechanical load transmission to the tibia was implemented by a rotatable holding block, an angled bone adapter, and a disposable bone pot, into which the tibial bone end was fixed. The bone adapters contained the bone pot and the angular spike at the base of the bone pot provided additional mechanical fixation of the femoral and tibial bone ends. On the **femoral side**, a threaded adapter component driven by an adjusting screw allowed the inclusion of knee joint specimens of variable length (range, 28–32 cm). Mechanical load transmission to the femur was realized in a similar, yet mirrored, configuration in the same way as on the tibial side, i.e. via rotatable holding block, angled bone adapter, and disposable bone pot. Angulations of the femoral and tibial bone adapters (0°, 5°, and 10°) brought the disposable bone pots (and the femur and tibia contained therein) into distinctly inclined positions. Thus, maximum knee joint flexion of 20° could be implemented under simultaneous axial compressive loading. Defined deviations of the mechanical axis could be set based on two separate mechanisms: i) On the **tibial and femoral sides**, the holding blocks were mounted on fixed fork mountings by means of studs that allowed for continuous rotation and variation of the mechanical axis in varus or valgus. Despite the holding blocks' rotatable mountings, their studs (and the chosen varus or valgus angles) were mechanically arrestable by a hexagon screw and nut. Precise setting of axis deviation could thus be carried out based on radial markings at 1° intervals on the mountings and holding blocks (range, 0–10° [varus] - 10° [valgus]). 2) Additionally, the set mechanical axis was secured by a varus-valgus

positioning unit at the **level of the joint**. To this end, two parallel abutments on the medial and lateral aspects of the joint were adjustable in the mediolateral plane along their threaded rods that were bilaterally centered between the peripheral counter-bearings and the central sliding block. Press-point discs fitted to the abutments could be adjusted in height as required by the individual knee joint specimen's anatomy and position. While this configuration allowed for variable positioning of the abutments in the X- and Y-planes, it also mechanically secured the chosen varus or valgus configuration and maintained it once set.

2.2.3. Control unit

Due to its MRI incompatibility, the control unit was located outside of the MRI scanner room and connected to the device via standard pressure lines. Analogous to an earlier device (Truhn et al., 2020), the control unit consisted of a digital-to-analogue converter (Multifunction I/O USB-6001, National Instruments, Austin, US) that was controlled by customized software routines implemented in LabVIEW (National Instruments). The control unit actuated a digital pressure valve (VPPM-6L-L-1-G18-0L6H-V1P-S1C1, Festo) that could be set to any target pressure levels from 0 to 4.69 bar. Resultant (theoretical) forces on the loading piston ranged from 0 to 1556 N. As detailed above (see **2.2.2 Loading Unit**), loading was rigidly transferred to the tibia by displacement towards the joint.

2.2.4. Calibration of set pressures vs. resultant forces

The axial compressive loading device and its digital control were mechanically validated using a digital hydraulic force gauge

(#HKMD29D, Induk, Wuppertal, Germany, specifications: pressure range 0–2.5 kN; accuracy $\pm 1.0\%$ [of full scale]) positioned between the tibial-sided holding block (empty) and a rigid PVC plate clamped between both arrested abutments. Resultant forces were determined as a function of increasing pressure levels set at intervals of 0.2 bar. These measurements were repeated three times and mean forces were calculated for each set pressure level. Pearson's correlation coefficient r was then determined using GraphpadPrism (version 5.0, GraphPAD Software Inc., San Diego, CA, USA). Moreover, we also assessed force levels as a function of time, i.e. longitudinally. To this end, mean force levels at constant pressure levels of 1.5 bar and 3 bar were determined every minute over a period of 30 min.

2.3. Human knee joint specimens

2.3.1. General information

In total, ten fresh and structurally intact human knee joint specimens were obtained from the Department of Anatomy (RWTH Aachen University, Germany) from body donors who had deceased due to unrelated medical conditions. The specimens' characteristics were 7 male and 3 female, 4 right and 6 left, and their mean age at death was 83.2 ± 8.5 years (range, 75–95 years). Knee joint specimens were frozen immediately after death and thawed at least 24 h prior to the measurements. At study initiation, local Institutional Review Board approval (Ethical Committee, RWTH Aachen University, AZ-EK180/16) and written informed consent by the body donors were available.

2.3.2. Preparation

In line with standard procedures, the human knee joint specimens were prepared to 28–32 cm length because of spatial restrictions in component positioning within the device. Shorter specimens were rejected, while longer specimens were cut to approximately 30 cm length by use of an electric saw. Then, the soft tissues around the resected femoral and tibial diaphysis were cleared at a length of approximately 5 cm using standard surgical scalpels (No. 11, Feather Safety Razor, Osaka, Japan). During these preparations, the fibula was shortened to prevent mechanical interference. Not yet mechanically fixed, the thus prepared femoral and tibial diaphyses were positioned in the bone pots with residual play. Once the specimen was settled in full extension and normal rotation, the exposed femoral and tibial bone ends were fixed in the bone pots using liquid polymethyl-methacrylate (Technovit 3040, Heraeus Kulzer GmbH, Wehrheim, Germany). Prior to curing, the spike attached at the bottom of the bone pot was driven into the cancellous bone for additional fixation. The bone-filled pots were inserted into the 0°-angled bone adapters and the entire knee joint specimen was aligned in the neutral position without force application. After curing, the 5°-angled bone adapters were used to bring the knee joint specimen in 10° knee flexion. Similarly, the varus-valgus positioning unit was adjusted so that the bilateral abutments and press-point discs were brought in line with the joint line and in loose contact with the specimen.

2.4. Imaging studies

2.4.1. MR imaging studies

Absence of relevant magnetic field inhomogeneity was determined by B_0 mapping of the device. To this end, a T2*-weighted 3D gradient echo sequence was acquired using the Q-body coil and the following sequence parameters: axial image orientation; TR [time to repetition] = 52 ms; TE [echo time] = 12 ms; flip angle = 20°; number of slices = 50; ST [slice thickness] = 7.5 mm; no SG [slice gap]; FOV [field of view] = 560 mm $\times$ 560 mm; AM [acquisition matrix] = 256 $\times$ 256; RM (reconstruction matrix) = 672 $\times$ 672; scan percentage = 78.5%; NSA [number of signal averages] = 3.

Loaded with a single knee joint specimen, the axial compressive loading device was then centrally positioned in the bore of a clinical

3.0T scanner (Achieva, Philips, Best, The Netherlands). For MR imaging, multi-purpose coils (Sense Flex L Dual Coils, Philips) circumferentially comprised the press-point discs at the medial and lateral aspect of the joint. The use of a dedicated multi-channel knee coil was not possible due to the device's overall configuration. After setting up and checking of operability, we carried out the MRI measurements in seven configurations per joint:

1) unloaded (δ_0),
2) neutrally aligned at 1.5 bar (=0.33 kN, δ_{neu1}),
3) neutrally aligned at 3.0 bar (=0.74 kN, δ_{neu2}),
4) 10° varus aligned at 1.5 bar (δ_{var1}),
5) 10° varus aligned at 3.0 bar (δ_{var2}),
6) 10° valgus aligned at 1.5 bar (δ_{vlg1}), and
7) 10° valgus aligned at 3.0 bar (δ_{vlg2}).

All measurements were performed in 10° knee flexion. Of note, overall joint integrity and largely preserved cartilage tissue thickness in both femorotibial compartments were orientationally checked at δ_0 before proceeding with the measurements. Two knee joint specimens with severe and wide-spread cartilage lesions and focal cartilage eburnation were excluded from the study after the δ_0 measurements. Following each change in pressure level, a 5 min pause was taken to allow for equilibration. For each configuration of the joint, the imaging protocol was completed, which included fat-saturated 2D Proton density-weighted sequences (PDw fs) and 3D water selective cartilage scans (WATSc). Please see Table 1 for details on sequence parameters. In clinical contexts, PDw fs sequences are commonly used for musculoskeletal imaging in general and for knee joint and articular cartilage assessment in particular (Gold et al., 2009; Rogers et al., 2013). For δ_0, PDw fs sequences were acquired in sagittal, axial, and coronal orientations, while for all loaded configurations (i.e. δ_{neu1}, δ_{neu2}, δ_{var1}, δ_{var2}, δ_{vlg1}, and δ_{vlg2}) only the axial and coronal sequences were acquired. In research contexts, WATSc sequences are used for performing cartilage segmentations and morphometric measurements at high resolutions (Eckstein et al., 2014). In our study, the sequence was obtained in the coronal orientation. Proper joint position and loading were checked based on multiplanar scout views. For each joint configuration, MRI measurements were performed in the order 1–7) as detailed above, and at room temperature, which was monitored during one measurement series (19.8 $\pm$ 0.9 °C).

Table 1
Acquisition Parameters of MR sequences.

	PDw fs	WATSc
Orientation	cor, ax (sag)	cor
Type of fat saturation	SPAIR	water-selective excitation
Sequence Type	Turbo spin echo	Gradient echo
Repetition Time [ms]	7125	9.6
Echo time [ms]	30	5.0
Turbo spin-echo factor	15	1
Field of view [mm]	180 × 180	180 × 180
Acquisition matrix	368 × 360	368 × 368
Reconstruction matrix	512 × 512	512 × 512
Scan percentage [%]	100	78.5
Flip angle [°]	90	17
Number of signal averages	1	1
Slices	30	266
Slice Thickness/Gap [mm]	3.0/3.3	1.5/0.75
Duration [min]	3 min 45 s - 6 min 30 s	9 min 30 s

PDw – proton density-weighted, WATSc - water selective cartilage scan, SPAIR - spectral attenuated inversion recovery, fs - fat-saturated, cor - coronal, ax - axial, sag - sagittal. In the unloaded reference configuration, the PDW fs sequences were obtained in the cor, ax, and sag orientations. In all loaded configurations, the PDW fs sequences were only obtained in the cor and ax orientations.

2.4.2. CT studies

Sequential CT scanning of the knee joint specimens was performed on a clinical multidetector-row CT scanner (SOMATOM Force, Siemens, Erlangen, Germany). Tube voltage was set to 120 kV, tube current to 800 mAs, and slice thickness to 0.6 mm. Further scan parameters were rotation time, 1 s; increment, 2 mm; pitch, 0.8. The field of view (FOV) was adapted to the topographic outline of the specimen within the device so that pixel size was 0.31 mm $\times$ 0.31 mm (FOV, 150 $\times$ 150 mm; matrix, 512 $\times$ 512). The scan duration was approximately 5.3 s per configuration. We used the Siemens kernel Br64s for image reconstructions in all three principal planes. Similar to the MRI measurements, the corresponding CT series were performed in the order 1–7).

2.5. Image analysis

2.5.1. MRI studies

The MRI data of the knee joint specimens were processed individually for each joint configuration. Chondrometrics software (Chondrometrics GmbH, Ainring, Germany) was used to obtain morphometric measurements of the femoral and tibial cartilage thickness in the medial and lateral femorotibial compartments, based on manual segmentation and subsequent computations as described previously (Wirth and Eckstein, 2008). Due to its excellent cartilage-bone and cartilage-fluid contrast, the coronal 3D WATS-c sequence was used for segmentation of the subchondral bone interface and cartilage surface. Experienced readers performed segmentation in each of the coronal images that displayed cartilage tissue while being blinded to the joint's configuration and remaining readings. An expert reader performed quality checks of segmentation quality. Based on the segmented bone interface and cartilage surface, 3D reconstructions of cartilage surface areas were generated and used to compute the mean cartilage thickness and related morphometric measures of cartilage over the subchondral bone. Cartilage thickness (ThC) was computed for the following cartilage plates and subregions: medial and lateral tibia (MT, LT), medial and lateral weight-bearing (i.e. central) femur (cMF, cLF), five subregions (anterior, posterior, central, external, and internal) of the MT and LT, and three subregions (internal, external, and central) of the cMF and cLF (Wirth and Eckstein, 2008). Of note, ThC was determined in each specimen, configuration, and (sub)region. The reliability of these measurements has been reported previously (Wirth and Eckstein, 2008).

In addition, meniscus extrusion (ExM) was determined for each joint configuration by determining the centres of the medial and lateral meniscus body at the midportion of the tibial plateau and by consecutively measuring the horizontal distance from the cartilage-covered tibial plateau's outermost (medial or lateral) aspect to the outermost edge of the base of the medial (MM) or lateral meniscus (LM) as published previously (Patel et al., 2016).

2.5.2. CT studies

For CT analyses, sagittal, coronal, and axial reconstructions were evaluated to quantify joint flexion and mechanical axis deviation in all joint configurations. To this end, the central sagittal slice was identified as the one that visualized the spikes within the femoral and tibial shafts to the greatest possible extent, while the central coronal slice was identified as the one that centrally bisected the weightbearing region of the femorotibial joint, i.e. at half of the anteroposterior distance between the deepest point of the trochlear groove and the posterior condylar line. On the central sagittal slice, joint flexion was quantified as the angle between the femoral and tibial shafts as measured using the inbuilt angle measuring tool of the clinical picture archiving and communications system (PACS, iSite, Philips) available in house. Similarly, mechanical axis deviation was measured on the central coronal slice as the angle between the femoral and tibial shaft. One investigator (MW, two years of experience in musculoskeletal imaging) performed these measurements for each joint configuration. Total blinding of the reader

was impossible as the joint's configuration in terms of alignment and loading intensity was easily discernible.

Shaded CT volume renderings were generated using IntelliSpace Clinical Applications (Philips) for the sake of visualizing the entire joint in all configurations.

2.6. Reference assessment

2.6.1. Histological Assessment

Following imaging, the human knee joint specimens underwent histological and biomechanical work-up. For the former, the joint was accessed through the medial parapatellar approach, the patella everted laterally, the collateral and cruciate ligament complex completely dissected, and the femoral and tibial joint surfaces thus fully exposed. The peripheral central (i.e. mid-coronal) weightbearing joint areas were sampled at the distal femoral condyles and proximal tibial plateau using an electric saw and a rongeur. Similarly, the central body region of the medial and lateral meniscus was sampled using a surgical scalpel. Sampled joint regions were cut to standard dimensions of ca. 2 $\times$ 2 cm (width x length) and tissue-marking dye (Polysciences, Warrington, US) was used to define the coronal plane (for consistent future reference) of these samples. Histological sections were prepared along this plane according to standard as before (Nebelung et al., 2018, 2019a, 2019b; Truhn et al., 2019). In brief, paraformaldehyde (4%) was used to fix meniscus samples, while Ossa fixona (Diagonal, Münster, Germany) was used for simultaneous decalcification and fixation of cartilage-bone samples. Upon embedding in paraffin, cutting to 5-μm sections, staining with hematoxylin/eosin and Safranin O, samples were imaged using a digital light microscope (BZ-9000, Keyence, Osaka, Japan). For visualization of the cartilage and meniscus samples in their entirety, two - six individual micrographs were merged into one image per sample. Two investigators (SN [fellowship trained, 11 years of experience in musculoskeletal histopathology]; MW [2 years of experience in musculoskeletal histopathology]) performed the semiquantitative histological grading. Cartilage samples were graded based on the Mankin classification (Mankin et al., 1971) by assessing structural (score 0–6), cellular (score 0–3), PG staining-associated (score 0–4), and tidemark-associated (score 0–1) tissue properties. Individual scores were summed to give the Mankin sum score (range, 0–14) that indicated the absence of degeneration by score 0 and most severe degeneration by score 14. Similarly, meniscus samples were graded based on the Pauli classification (Pauli et al., 2011). Briefly, the Pauli classification assesses surface integrity for the femoral, tibial, and inner meniscal surfaces (score 0–3 each, i.e. 0-9), cellularity (score 0–3), collagen organization (score 0–3), and matrix staining (score 0–3). Analogously, the range of Pauli sum scores is 0–18 with 0 indicating no degeneration (score 0) and 18 indicating most severe degeneration. Both investigators graded the tissues individually and on a per-sample basis. Final scores were discussed until consensus was reached, thus, no measures of inter- or intra-rater variability was calculated.

2.6.2. Biomechanical assessment

For biomechanical reference assessment, cartilage samples were harvested from the sampled medial and lateral femoral and tibial joint surfaces (see 2.6.1 Histological Assessment) but were not fixed but processed fresh. As published earlier (Nebelung et al., 2017b), a skin biopsy punch (diameter: 8 mm; pfm-medical, Cologne, Germany) was used to cut cylindrical chondral samples from the cartilage-bone material. The subchondral bone was removed from the cartilage-bone interface by use of a surgical scalpel to obtain samples of uniform thickness. Upon determination of sample thickness by digital micrometry (Mitutoyo 293–521; Mitutoyo, Tokyo, Japan), chondral samples underwent unconfined compression tests on a universal mechanical testing machine (Zwick/Roell Z2.5; Zwick/Roell, Ulm, Germany) equipped with a compressive piston (diameter: 20 mm) and a load cell (force range: 200 N). In practical terms, samples were compressed to a

maximum strain of 21% at a constant displacement rate of 0.15% strain/sec. The response to loading of cartilage depends on the complex interplay of fluid pressurization and fibril reinforcement. This strain rate was chosen because of its time efficiency and assesses the former's contribution over the latter (Li and Herzog, 2004). Displacement and load data were simultaneously recorded using TestXpert software (Zwick/Roell) and used to determine Instantaneous Young modulus (IYM) as the ratio of stress and strain within the strain range of 10–20%. To this end, a tangent was fitted to this strain range to determine the specific chondral sample's IYM. In total, four cartilage samples were prepared per knee joint specimen, i.e. femoral medial and lateral as well as tibial medial and lateral. These were always kept hydrated.

2.6.3. Force validation

Following imaging, femorotibial pressure mappings were performed for each configuration in four of the human knee joint specimens. Digital electronic pressure-sensitive sensors (K-Scan 4000, 10.000 psi, Tekscan, Boston, MA, US; further specifications: pressure-sensitive area, 33×27.9 mm [height x width]; number of sensor elements/cm^2, 62; maximum pressure level, 68948 kPa; thickness, 0.1 mm) were used as in earlier studies that investigated static pressure distributions in human knee joints (Agneskirchner et al., 2007; Suero et al., 2017). In practical terms, the joints were accessed as detailed above (see 2.6.1 Histological Assessment) and in two of the four joints, the cruciate ligament complex had to be partially cut for full access to the joint. The sensors were then inserted into the medial and lateral femorotibial compartments above the menisci while attention was paid to avoid crinkling or displacement. The sensors were positioned to cover the anterior and central weight-bearing regions of the medial and lateral femoral condyles. Yet, coverage of the femur was limited to the anterior two-thirds of the tibiofemoral articular surface due to limitations in the sensor area. Following preconditioning and calibration as recommended by the manufacturer, total force levels were determined in all configurations. Of note, equilibration periods of 5 min were observed after changing the pressure level or joint configuration and no intraarticular forces were detected at δ0. In total, forces on the entire femorotibial joint were measured three times after sensor repositioning and equilibration. Forces as output by the sensors were recorded and averaged.

2.7. Statistical analysis

Statistical analysis was performed by the senior author (SN) using GraphpadPrism. In the following, δ0 gives the parameter value in the unloaded reference configuration, while δ_{neu1}, δ_{neu2}, δ_{var1}, δ_{var2}, δ_{vlg1}, and δ_{vlg2} refer to the parameter values in the six loaded joint configurations 1–7) as defined above. Relative changes were calculated by relating the parameter values to δ0.

Parametric tests were chosen as morphometric cartilage and meniscus measures as well as histological and biomechanical measures were assumed to be normally distributed. Hence, repeated-measures ANOVA followed by Tukey's post-hoc test was applied to assess differences between the joint configurations, while one-way ANOVA was used to assess differences in the histological and biomechanical reference measures between the four cartilage plates, i.e. medial/lateral and femoral/tibial. Correspondingly, paired Student's t-test was used to assess differences between histological Pauli sum scores of the two menisci within the joint. Correlations between relative changes in ThC and histological as well as biomechanical measures were assessed per cartilage plate using Spearman's correlation coefficient. Data are given as means ± standard deviation. Due to our study's exploratory nature, the Bonferroni correction was applied to correct for multiple comparisons and to adjust for alpha inflation. Hence, the level of significance was set to $p \leq 0.05/20 = 0.0025$ as cartilage thickness was assessed in four joint regions and five tibial as well as three femoral subregions, respectively. This 'stricter-than-usual' level of significance was intended to contain the number of statistically significant, yet scientifically

(likely) irrelevant findings.

3. Results

Validation studies of axial force generation revealed a highly linear association with set pressure levels ($y = 0.264*x - 0.063$; $r^2 = 0.999$), where x is the pressure applied, and y the resultant force level. Accordingly, set pressure levels of 1.5 bar and 3 bar resulted in forces of 0.33 ± 0.02 kN (= 33.7 kg) and 0.74 ± 0.01 kN (= 75.5 kg), respectively. Longitudinal force evaluation at set pressure levels of 1.5 bar and 3 bar revealed constant force levels and no loss in force.

Total forces within the joints revealed significantly different absolute forces of 0.12 ± 0.02 kN (δ_{neu1}), 0.39 ± 0.09 kN (δ_{neu2}), 0.37 ± 0.07 kN (δ_{var1}), 0.59 ± 0.09 kN (δ_{var2}), 0.37 ± 0.04 kN (δ_{vlg1}), and 0.63 ± 0.09 kN (δ_{vlg2}) ($p < 0.0001$) in the different joint configurations. In the δ_{var1} and δ_{var2} configurations, the medial joint compartment was loaded exclusively, while the lateral joint compartment was distended and not pressurized at all. The opposite was observed for the δ_{vlg1} and δ_{vlg2} configurations.

All human knee joint specimens underwent complete MRI and CT scanning according to protocol (all joint configurations), and no adverse or unexpected events occurred. In qualitative terms, the medial and lateral femorotibial compartments were homogeneously compressed in the neutral axis. As indicated by progressive exudation of intraarticular compartmental synovial fluid, the extent of pressurization was clearly related to loading intensity. Cartilage thickness and volume became smaller with higher loading intensity (Fig. 2a–e). In varus alignment, the medial femorotibial compartment was compressed, while the lateral compartment was distended. In valgus alignment, however, the lateral compartment was compressed, while the medial compartment was distended (Fig. 2f–i).

In quantitative terms, loading-induced changes in cartilage morphometry, i.e. ThC, were reflective of the biomechanical loading conditions in terms of intensity and alignment. In both compartments, ThC decreased significantly in response to loading, both at compartmental, regional and sub-regional level. Tables 2 and 3 indicate regional and sub-regional changes in ThC, while Table 4 gives details of the post-hoc analysis. More intense loading induced more substantial changes in ThC, e.g. cMF (relative change in ThC vs. δ0 [%]): δ_{neu1}, -2.1%; δ_{neu2}, -4.6%; δ_{var1}, -4.9%; δ_{var2}, -8.8%; δ_{vlg1}, -1.5%; δ_{vlg2}, 3.3% ($p < 0.0001$); cLF: δ_{neu1}, -1.2%; δ_{neu2}, -3.9%; δ_{var1}, -4.9%; δ_{var2}, -2.0%; δ_{vlg1}, -6.5%; δ_{vlg2}, -9.4% ($p < 0.0001$). Quantitatively, relative changes in ThC were related to loading intensities to further elucidate the relation between both variables. When referencing relative changes in ThC [%] to applied loading intensities [kN], the following values of the relative changes in ThC per kN [%/kN] were found: medial femorotibial compartment, δ_{neu1}, -16%/kN; δ_{neu2}, -10%/kN; δ_{var1}, -14%/kN; δ_{var2}, -14%/kN; δ_{vlg1}, -4%/kN; δ_{vlg2}, 5%/kN; lateral femorotibial compartment; δ_{neu1}, -12%/kN %; δ_{neu2}, -12%/kN; δ_{var1}, -14%/kN; δ_{var2}, -3%/kN; δ_{vlg1}, -20%/kN; δ_{vlg2}, -17%/kN. Of note, if not directly loaded (e.g. the medial compartment in valgus alignment), the respective compartment's morphometric parameters remained largely unchanged, even though slight increases in ThC were found alongside slight decreases (Tables 2 and 3).

Detailed analyses of femoral and tibial subregions are given in Tables 3 and 4 Except for the posterior lateral tibial and internal central femoral subregions, all subregions displayed decreases in ThC under loading. In neutral alignment, the distribution and magnitude of relative changes were quite variable with the central subregions displaying the largest changes both medially and laterally. In valgus alignment, changes were most prominent in the external subregion of the central lateral femur and throughout the entire lateral tibia (except for the posterior subregion). Correspondingly, in varus alignment, changes were largest in the central and external subregions of both medial femur and tibia.

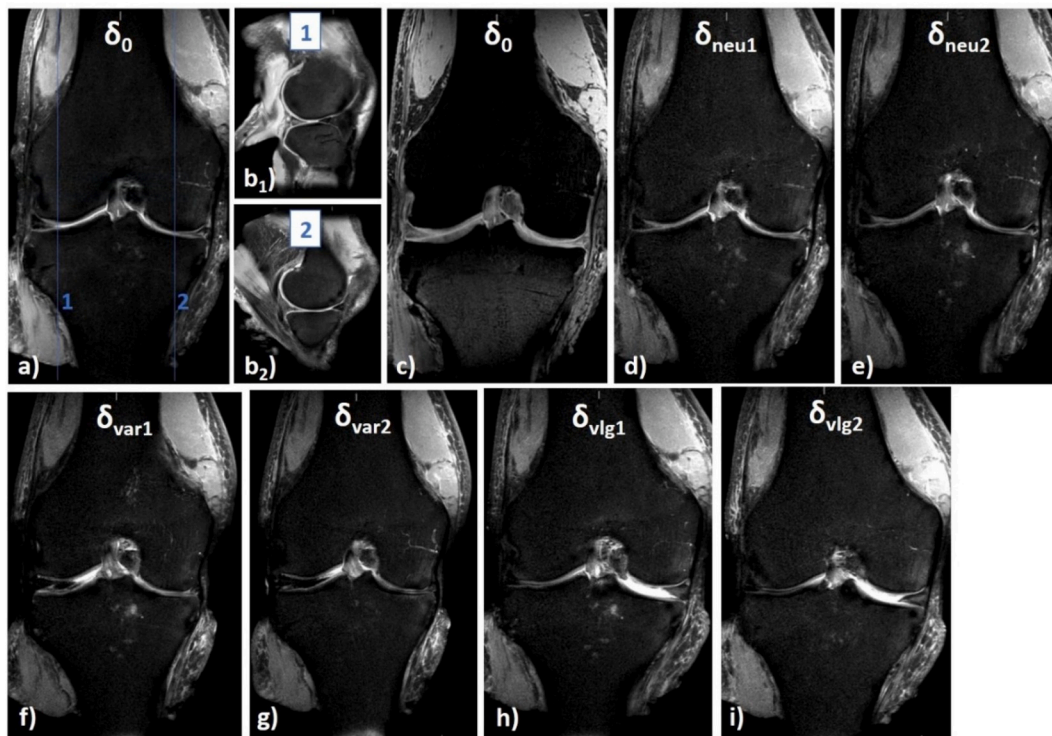Meniscus extrusion increased significantly in response to loading,

Fig. 2. Representative MR images of a right human knee joint undergoing standardized compressive loading at variable intensities and mechanical axis deviations. a-c) MR images of the unloaded configuration (δ_0) and in the coronal (a, c) and sagittal orientations (b). Coronal images were obtained through the central weight-bearing region of the femur (a, c) and the central lateral (b_1) and medial (b_2) femorotibial joint compartments as indicated by the numbered blue lines. The posterior horns of the lateral and medial menisci displayed signs of severe meniscopathy with surface disintegration, while gross tissue tearing was only found in the medial meniscus (femoral surface). Otherwise, the knee joint was structurally largely intact. d-i) Mid-coronal MR images (as in a, c) in response to increasing loading of 0.33 kN (δ_{neu1} [d]) and 0.74 kN (δ_{neu2} [e]) in the neutral axis. Analogously, equal loading intensities were applied to the joint in 10° varus alignment (δ_{var1} [f] and δ_{var2} [g]) as well as in 10° valgus alignment (δ_{vlg1} [h] and δ_{vlg2} [i]). While the joint was homogeneously compressed in the neutral axis, it was compartmentally compressed in varus and valgus alignment with the medial (in varus) and lateral (in valgus) compartments undergoing substantial compression while the contralateral compartments were grossly distended. All images are proton density-weighted and fat saturated, except for the WATSc sequence used for cartilage segmentation and morphometric analyses (c).

Table 2
Mean thickness [mm^3] of medial and lateral tibial and femoral articular cartilage regions of human knee joints (n = 10) as a function of variable loading intensities and mechanical axis deviations.

		δ_0	δ_{neu1}	δ_{neu2}	δ_{var1}	δ_{var2}	δ_{vlg1}	δ_{vlg2}	p-value
Medial Compartment	Tibia	1.52 ± 0.15	1.50 ± 0.16 (−1.7 ± 2.6)	1.47 ± 0.15 (−3.4 ± 3.2)	1.44 ± 0.14 (−5.7 ± 2.3)	1.41 ± 0.13 (−7.7 ± 3.3)	1.55 ± 0.17 (−1.4 ± 3.4)	1.56 ± 0.14 (2.4 ± 3.4)	< **0.0001** **[1]**
	Femur	1.51 ± 0.27	1.48 ± 0.30 (−2.3 ± 5.1)	1.44 ± 0.20 (−4.5 ± 3.8)	1.44 ± 0.28 (−5.1 ± 3.7)	1.38 ± 0.29 (−9.0 ± 7.7)	1.53 ± 0.35 (0.7 ± 6.8)	1.56 ± 0.32 (2.9 ± 4.4)	< **0.0001** **[2]**
Lateral Compartment	Tibia	1.80 ± 0.28	1.77 ± 0.30 (−1.8 ± 2.9)	1.70 ± 0.29 (−5.4 ± 3.6)	1.69 ± 0.30 (−5.9 ± 3.4)	1.77 ± 0.30 (−1.7 ± 3.1)	1.65 ± 0.30 (−8.6 ± 5.4)	1.58 ± 0.24 (−11.8 ± 4.6)	< **0.0001** **[3]**
	Femur	1.60 ± 0.18	1.58 ± 0.20 (−1.2 ± 3.6)	1.54 ± 0.19 (−3.9 ± 5.1)	1.52 ± 0.20 (−5.0 ± 4.5)	1.57 ± 0.22 (−2.2 ± 4.3)	1.50 ± 0.20 (−6.6 ± 5.4)	1.45 ± 0.18 (−9.3 ± 4.8)	< **0.0001** **[4]**

Joint configurations are as follows: unloaded (δ_0), neutral alignment and set pressure level of 1.5 bar (δ_{neu1}), neutral alignment and 3.0 bar (δ_{neu2}), 10° valgus alignment and 1.5 bar (δ_{vlg1}), 10° valgus alignment and 3.0 bar (δ_{vlg2}), 10° varus alignment and 1.5 bar (δ_{var1}), and 10° varus alignment and 3.0 bar (δ_{var2}). Data are given as mean ± standard deviation and (percentage change as compared to δ_0 [%] [mean ± standard deviation]). Statistical analysis was performed by repeated-measures ANOVA. Tukey's post-hoc testing details as indicated by square brackets [1–4] may be found in Table 4.

both for the MM (extrusion [mm], 3.7 ± 1.4 [δ_0]; 4.3 ± 1.2 [δ_{neu1}]; 4.8 ± 1.6 [δ_{neu2}]; 4.5 ± 1.2 [δ_{var1}]; 4.6 ± 1.3 [δ_{var2}]; 3.2 ± 1.4 [δ_{vlg1}]; and 3.2 ± 1.3 [δ_{vlg2}]; p < 0.0001) and for the LM (extrusion [mm], 2.3 ± 0.8 [δ_0]; 2.8 ± 0.7 [δ_{neu1}]; 3.0 ± 0.8 [δ_{neu2}]; 1.5 ± 1.5 [δ_{var1}]; 1.6 ± 1.5 [δ_{var2}]; 2.9 ± 0.6 [δ_{vlg1}]; and 2.8 ± 0.9 [δ_{vlg2}]; p < 0.0001).

Reference assessment by CT revealed hardly any joint space narrowing in response to compressive loading in the neutral axis, while the medial (and lateral) joint spaces were compressed in varus and valgus alignment, indicating compartmental pressurization and compression (Fig. 3).

When assessing coronal and sagittal alignment under loading we made the following observations. First, the mechanical axes (as assessed on the central coronal slices) remained largely unchanged during loading in the neutral alignment (coronal angles [°], 0.5 ± 1.3 [δ_0]; 0.8 ± 1.5 [δ_{neu1}]; 1.2 ± 1.9 [δ_{neu2}]; p = 0.026) with slight valgus angulation maintained throughout. In contrast, coronal angles were significantly different from the unloaded configuration in varus and valgus alignment (varus: 7.4 ± 1.3 [δ_{var1}], 7.3 ± 0.9 [δ_{var2}], p < 0.001; valgus: 9.7 ± 1.1 [δ_{vlg1}]; 9.4 ± 0.8 [δ_{vlg2}]; p < 0.001). In contrast, joint flexion angles did not change significantly throughout the different joint configurations (sagittal angles [°], 10.6 ± 2.0 [δ_0]; 11.0 ± 2.3 [δ_{neu1}]; 11.2 ± 1.9 [δ_{neu2}]; 11.6 ± 1.5 [δ_{var1}]; 11.8 ± 1.6 [δ_{var2}]; 11.1 ± 1.7 [δ_{vlg1}]; 11.2 ±

Table 3
Mean thickness of the medial and lateral tibial and femoral articular cartilage subregions as a function of variable loading intensities and mechanical axis deviations.

			δ_0	δ_{neu1}	δ_{neu2}	δ_{var1}	δ_{var2}	δ_{vlg1}	δ_{vlg2}	p-value
Medial Compartment	Tibia	central subregion of MT	2.02 ± 0.25	1.96 ± 0.28 (−3.2 ± 4.7)	1.90 ± 0.29 (−5.9 ± 6.7)	1.84 ± 0.25 (−8.7 ± 5.0)	1.78 ± 0.24 (−11.8 ± 6.4)	2.04 ± 0.29 (1.2 ± 6.3)	2.10 ± 0.28 (4.0 ± 6.2)	<0.0001 [5]
		external subregion of MT	1.22 ± 0.16	1.20 ± 0.17 (−1.7 ± 6.5)	1.16 ± 0.19 (−5.3 ± 8.6)	1.09 ± 0.16 (−10.9 ± 6.4)	1.04 ± 0.14 (−14.9 ± 7.2)	1.26 ± 0.21 (3.0 ± 7.5)	1.27 ± 0.16 (3.9 ± 5.4)	**< 0.0001 [6]**
		internal subregion of MT	1.71 ± 0.21	1.71 ± 0.23 (0.0 ± 2.4)	1.70 ± 0.22 (−0.6 ± 3.9)	1.64 ± 0.20 (−3.9 ± 3.8)	1.64 ± 0.20 (−4.0 ± 3.9)	1.77 ± 0.22 (3.3 ± 4.3)	1.76 ± 0.21 (2.7 ± 4.5)	**< 0.0001 [7]**
		anterior subregion of MT	1.51 ± 0.14	1.49 ± 0.15 (−1.0 ± 3.3)	1.47 ± 0.16 (−2.4 ± 3.4)	1.46 ± 0.15 (−3.3 ± 2.8)	1.44 ± 0.16 (−4.9 ± 4.6)	1.51 ± 0.16 (−0.3 ± 2.5)	1.52 ± 0.13 (0.8 ± 4.2)	**0.0012 [8]**
		posterior subregion of MT	1.21 ± 0.15	1.18 ± 0.15 (−2.4 ± 2.4)	1.18 ± 0.15 (−2.6 ± 2.9)	1.18 ± 0.16 (−2.8 ± 3.6)	1.16 ± 0.15 (−4.5 ± 3.1)	1.23 ± 0.17 (0.9 ± 3.2)	1.23 ± 0.14 (1.3 ± 4.6)	**< 0.0001 [9]**
	Femur	central subregion of cMF	1.81 ± 0.38	1.74 ± 0.42 (−3.9 ± 5.8)	1.68 ± 0.37 (−7.3 ± 4.7)	1.72 ± 0.42 (−5.7 ± 6.2)	1.62 ± 0.44 (−11.2 ± 10.5)	1.83 ± 0.50 (0.2 ± 9.2)	1.88 ± 0.46 (3.1 ± 5.7)	**< 0.0001 [10]**
		external subregion of cMF	1.24 ± 0.18	1.20 ± 0.17 (−2.6 ± 5.1)	1.18 ± 0.17 (−4.7 ± 5.5)	1.13 ± 0.15 (−8.1 ± 5.7)	1.09 ± 0.17 (−11.7 ± 7.3)	1.22 ± 0.25 (−1.9 ± 7.7)	1.25 ± 0.21 (1.0 ± 6.5)	**< 0.0001 [11]**
		internal subregion of cMF	1.50 ± 0.29	1.50 ± 0.33 (−0.4 ± 5.2)	1.48 ± 0.28 (−1.2 ± 3.9)	1.47 ± 0.30 (−2.0 ± 3.5)	1.43 ± 0.30 (−4.4 ± 6.9)	1.56 ± 0.35 (3.3 ± 5.8)	1.57 ± 0.34 (4.3 ± 4.3)	**< 0.0001 [12]**
Lateral Compartment	Tibia	central subregion of LT	2.66 ± 0.55	2.61 ± 0.59 (−2.0 ± 4.9)	2.45 ± 0.62 (−8.5 ± 7.5)	2.45 ± 0.61 (−8.4 ± 6.2)	2.60 ± 0.61 (−2.7 ± 5.4)	2.33 ± 0.62 (−13.3 ± 10.4)	2.18 ± 0.54 (−18.4 ± 8.4)	**< 0.0001 [13]**
		external subregion of LT	1.35 ± 0.24	1.33 ± 0.25 (−1.4 ± 3.1)	1.31 ± 0.25 (−3.3 ± 3.8)	1.33 ± 0.25 (−1.3 ± 5.2)	1.38 ± 0.25 (2.0 ± 5.9)	1.23 ± 0.20 (−8.7 ± 5.6)	1.18 ± 0.17 (−12.3 ± 5.6)	**< 0.0001 [14]**
		internal subregion of LT	1.81 ± 0.30	1.76 ± 0.33 (−2.9 ± 3.9)	1.67 ± 0.36 (−8.1 ± 6.4)	1.68 ± 0.35 (−7.7 ± 6.2)	1.75 ± 0.32 (−3.8 ± 3.3)	1.65 ± 0.36 (−9.2 ± 8.1)	1.62 ± 0.33 (−10.9 ± 7.2)	**< 0.0001 [15]**
		anterior subregion of LT	1.56 ± 0.22	1.53 ± 0.22 (−2.0 ± 2.9)	1.51 ± 0.18 (−3.4 ± 3.9)	1.47 ± 0.15 (−5.6 ± 7.3)	1.50 ± 0.19 (−3.4 ± 6.1)	1.46 ± 0.17 (−5.9 ± 4.6)	1.38 ± 0.13 (−10.9 ± 9.4)	**< 0.0001 [16]**
		posterior subregion of LT	1.62 ± 0.36	1.62 ± 0.38 (−0.7 ± 4.0)	1.59 ± 0.35 (−2.3 ± 3.3)	1.56 ± 0.40 (−4.5 ± 6.5)	1.64 ± 0.42 (0.2 ± 6.7)	1.56 ± 0.42 (−4.3 ± 7.5)	1.57 ± 0.38 (−3.8 ± 6.2)	0.062
	Femur	central subregion of cLF	1.92 ± 0.28	1.90 ± 0.29 (−0.9 ± 4.9)	1.85 ± 0.29 (−3.5 ± 7.1)	1.83 ± 0.29 (−4.6 ± 5.9)	1.90 ± 0.32 (−1.3 ± 6.5)	1.82 ± 0.30 (−5.2 ± 7.7)	1.75 ± 0.27 (−8.5 ± 7.2)	**< 0.0001 [17]**
		external subregion of cLF	1.42 ± 0.19	1.39 ± 0.21 (−2.8 ± 3.7)	1.35 ± 0.21 (−5.6 ± 5.0)	1.33 ± 0.21 (−6.9 ± 4.7)	1.38 ± 0.24 (−3.5 ± 5.8)	1.24 ± 0.19 (−12.9 ± 3.8)	1.17 ± 0.16 (−17.6 ± 5.0)	**< 0.0001 [18]**
		internal subregion of cLF	1.48 ± 0.13	1.48 ± 0.15 (−0.1 ± 3.6)	1.44 ± 0.11 (−2.8 ± 4.2)	1.43 ± 0.13 (−3.5 ± 3.8)	1.45 ± 0.14 (−1.9 ± 3.4)	1.45 ± 0.15 (−2.3 ± 5.8)	1.44 ± 0.15 (−2.5 ± 5.2)	0.055

Human knee joints (n = 10) were subject to variable loading conditions. MT - medial tibia. cMF - central medial femur. LT - lateral tibia. cLF - central lateral femur. Statistical analysis was performed using repeated-measures ANOVA. Wherever appropriate, post-hoc test details are numbered in square brackets [5–18] and detailed in Table 4. Please see Table 2 for additional details on joint configurations, their connotations, and details on data presentation.

2.0 [δ_{vlg2}]; p = 0.887).

Biomechanical evaluation of the sampled cartilage areas revealed no significant location-dependent differences in the tissue's biomechanical properties. IYM was determined as 2.77 ± 1.97 MPa (MT), 2.35 ± 1.81 MPa (LT), 3.51 ± 2.86 MPa (MF), and 3.68 ± 1.98 MPa (LF) (p = 0.094). However, variability was substantial with individual samples being very soft to very stiff as demonstrated by the wide range of IYM values (0.10 MPa–8.28 MPa).

Histologically, cartilage samples were largely grossly intact to mildly degenerative. Mean Mankin sum scores were 2.2 ± 0.8 (range, 1–3) for the LF, 1.7 ± 1.1 (range, 0–3) for the LT, 3.2 ± 1.3 (range, 1–5) for the MF, and 3.1 ± 0.9 (range, 2–5) for the MT (p = 0.011), indicating considerably more advanced cartilage degeneration in the medial than in the lateral femorotibial joint compartment. Qualitative evaluation revealed slight-to-moderate signs of degeneration in the grossly intact samples such as focal surface disintegration, hypercellularity and mild-to-moderate proteoglycan de-staining originating at the sample surface. In the more degenerative samples, we observed more severe signs of degeneration, too, such as widespread cellular cloning, surface tearing and clefting, pannus reformation and superficial tissue loss.

Meniscus samples were found to be of variable degeneration. With mean Pauli sum scores of 8.2 ± 2.3 (range, 5–12) for the LM and 4.3 ± 1.7 (range, 2–7) for the MM (p = 0.004), differences between the femorotibial compartments were significant. Consequently, LM samples displayed more severe and widespread signs of degeneration such as widespread surface disintegration and fibrillation, substantial fraying of the apex, areal hyper-to hypocellularity, disorganization of the extra-cellular matrix, signs of fibrocartilaginous separation, and moderate-to-strong proteoglycan staining. MM samples demonstrated signs of less severe degeneration.

Details of intra-specimen and intra-regional correlations between histological and biomechanical reference measures of cartilage and relative changes in regional ThC as well as between histological meniscus measures and relative changes in ExM are indicated in the Supplementary Tables 1 and 2

4. Discussion

The most important finding of the present study is that imaging biomarkers such as cartilage thickness are reflective of the biomechanical framework conditions applied during standardized compressive *in-situ* loading of human knee joints, while they are not related to histological and biomechanical measures.

In a first step, we designed, manufactured, and validated a dedicated

Table 4
Tukey's post-hoc testing details after repeated measures ANOVA as detailed by consecutive numbers [in square brackets] in Tables 2 and 3 Significant pair-wise differences are marked by asterisks and stratified according to [***], $p < 0.001$; [**], $0.001 \leq p < 0.01$; [*], $0.01 \leq p < 0.05$; [ns], non-significant.

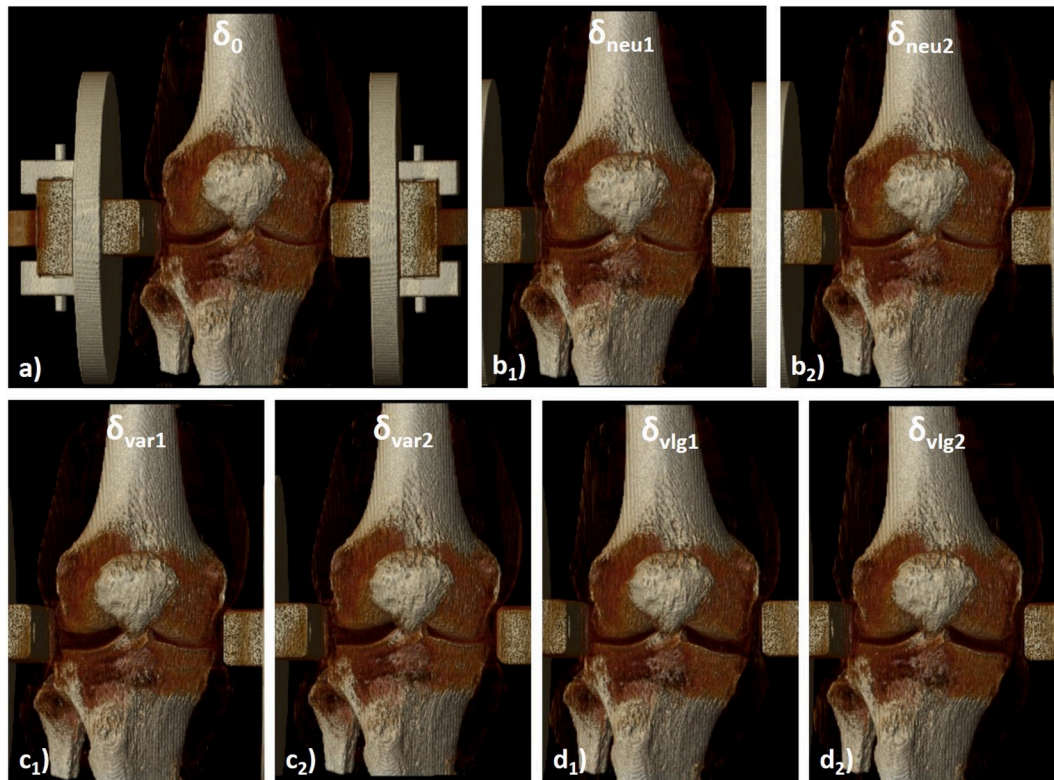|	[1]	[2]	[3]	[4]	[5]	[6]	[7]	[8]	[9]	[10]	[11]	[12]	[13]	[14]	[15]	[16]	[17]	[18]
δ_0 vs. δ_{neu1}	ns	ns	ns	ns	ns	ns	ns	ns	ns	ns	ns	ns	ns	ns	ns	ns	ns	ns
δ_0 vs. δ_{neu2}	ns	ns	**	ns	ns	ns	ns	ns	ns	ns	ns	ns	**	ns	**	ns	ns	*
δ_0 vs. δ_{vlg1}	ns	ns	***	***	ns	ns	ns	ns	ns	ns	ns	ns	***	**	***	ns	ns	***
δ_0 vs. δ_{vlg2}	ns	ns	***	***	ns	ns	ns	ns	ns	ns	ns	ns	***	***	***	***	***	***
δ_0 vs. δ_{var1}	***	ns	**	**	**	***	*	ns	ns	ns	*	ns	**	ns	**	ns	ns	**
δ_0 vs. $\delta var2$	***	***	ns	ns	***	***	*	*	**	**	***	ns	ns	ns	ns	ns	ns	ns
δ_{neu1} vs. δ_{neu2}	ns	ns	ns	ns	ns	ns	ns	ns	ns	ns	ns	ns	ns	ns	ns	ns	ns	ns
δ_{neu1} vs. δ_{vlg1}	ns	ns	***	**	ns	ns	ns	ns	ns	ns	ns	ns	***	*	*	ns	ns	***
δ_{neu1} vs. δ_{vlg2}	*	ns	***	***	*	ns	ns	ns	ns	ns	ns	ns	***	***	**	***	***	***
δ_{neu1} vs. δ_{var1}	*	ns	ns	ns	ns	**	*	ns	ns	ns	ns	ns	ns	ns	ns	ns	ns	ns
δ_{neu1} vs. δ_{var2}	***	*	ns	ns	**	***	*	ns	ns	ns	**	ns	ns	ns	ns	ns	ns	ns
δ_{neu2} vs. δ_{vlg1}	**	*	ns	ns	*	*	*	ns	ns	*	ns	ns	ns	ns	ns	ns	ns	***
δ_{neu2} vs. δ_{vlg2}	***	**	***	**	***	**	ns	ns	*	***	ns	*	***	***	ns	**	ns	***
δ_{neu2} vs. δ_{var1}	ns	ns	ns	ns	ns	ns	ns	ns	ns	ns	ns	ns	ns	ns	ns	ns	ns	ns
δ_{neu2} vs. δ_{var2}	**	ns	ns	ns	ns	**	*	ns	ns	ns	ns	ns	ns	ns	ns	ns	ns	ns
δ_{vlg1} vs. δ_{vlg2}	ns	ns	ns	ns	ns	ns	ns	ns	ns	ns	ns	ns	ns	ns	ns	ns	ns	*
δ_{vlg1} vs. δ_{var1}	***	*	ns	ns	***	***	***	ns	ns	ns	ns	*	ns	**	ns	ns	ns	**
δ_{vlg1} vs. δ_{var2}	***	***	***	*	***	***	***	*	***	***	**	***	***	***	ns	ns	ns	***
δ_{vlg2} vs. δ_{var1}	***	**	***	*	***	***	***	ns	*	*	**	**	***	***	ns	ns	ns	***
δ_{vlg2} vs. δ_{var2}	***	***	***	***	***	***	***	**	***	***	***	***	***	***	**	**	***	***
δ_{var1} vs. δ_{var2}	ns	ns	*	ns	ns	ns	ns	ns	ns	ns	ns	ns	ns	ns	ns	ns	ns	ns

Fig. 3. Shaded CT volume renderings of a right human knee joint undergoing standardized compressive loading. As compared to the unloaded configuration (a), loading-induced compression of the joint space was hardly discernible in the neutral axis (b), while medial and lateral joint space narrowing was considerably more prominent in response to compressive loading in varus (c) and valgus (d) alignment. The knee joint as the volume-of-interest was rotated and angulated for un-obstructed visualization of the joint space. The knee joint is the same as in Fig. 2; please also refer to Fig. 2 for a more detailed explanation of the joint configurations.

axial compressive loading device to apply compressive loading of variable intensity and alignment along the joint axis in an MRI-compatible manner. For the sake of reproducibility and standardization, loading was controlled by set pressure levels. We performed the measurements at set pressure levels of 1.5 bar and 3 bar, resulting in theoretical compressive forces of 0.50 kN and 1.00 kN, respectively. Pressure-force measurements indicated actual mean compressive forces to be substantially lower at 0.33 kN (33.7 kg) and 0.74 kN (75.5 kg), most likely secondary to unavoidable air leakage of the experimental setup. These forces are approximately equivalent to half and full standard body weight in the Western world (Walpole et al., 2012). Of note, even though the setup had been laid out to take substantially larger forces of up to twice standard body weight, such loading conditions were not implemented to avoid over-pressurization and potential damage. In earlier comparable studies by our group and others, loading was controlled by displacement (Nebelung et al., 2017a, 2017b, 2018, 2019b; Truhn et al.,

2019; Wang et al., 2015) or by pressure levels using specifically designed pneumatics (Chan et al., 2016; Wang et al., 2015; Zevenbergen et al., 2018). Displacement-controlled approaches incur stress relaxation and limit standardization of lengthy imaging protocols. This fact renders pressure-controlled approaches a more suitable choice for reasons of standardisation and intra- and inter-subject comparability in scientific and clinical contexts, even though a consensus on whether joint and/or tissue loading should be static or dynamic has not been reached yet.

In our study, longitudinal pressure-force validation revealed standardized pressurization of the femorotibial joint throughout the sequence acquisition period and no loss in force. However, we had to strike a balance between realizing effective loading in terms of force application, transmission, and absorption, and allowing sufficient freedom for physiological adaptations of the joint under loading. Hence, the relatively rigid experimental setup in terms of limited degrees of freedom of femur and tibia and constrained femur-tibia relations does not fully reflect the biomechanical boundary conditions of the human knee joint encountered *in vivo*.

Conceptionally, several mechanisms were implemented to maintain the joint in a physiological configuration during loading. Among these, the adjustable press-point disks, the spike-augmented (initially rotatable) fixation of the bone shafts in the bone pot, the rotatable holding blocks, mountings, and bone adapters and the axial length adjustment were intended to adapt the experimental setup to inherent differences in joint anatomy and physiology and to counter constraining forces, forced postures, and unphysiological joint configurations during loading. While our setup is likely to have emulated the tibiofemoral joint pressures and forces encountered when axially loading the joint during standing or walking, its physiological correspondence remains limited when considering the complexities involved in physiological knee joint kinetics. *In vivo*, considerable biomechanical moments are taken up by dynamic joint stabilizers such as muscles, which could not be considered in our setup (Winby et al., 2009).

Our axial compressive loading device only assessed the contributions of static stabilizers such as cruciate and collateral ligaments, the joint capsule, and the menisci. Accordingly, our experimental setup was laid out to standardize the biomechanical framework conditions of compressive loading in an MRI-compatible manner, rather than addressing all biomechanical complexities of *in-vivo* loading.

Pressure-controlled loading induced compression of the femorotibial joint that was bicompartmental in neutral alignment and compartmental in axis deviation, i.e. the medial or lateral femorotibial compartments were exclusively compressed in varus or valgus loading, respectively. Morphometric cartilage measures are indicative of these intra-articular changes. In neutral alignment, absolute femorotibial forces and relative changes in ThC were significantly lower than in varus or valgus alignment, which confirms earlier studies assessing the effects of altered mechanical alignment on compartmental contact pressures (Agneskirchner et al., 2007; Suero et al., 2015). Relative changes of the femoral and tibial cartilage were larger with higher loading intensities across all alignments, which is plausible considering the tissue's essential role in weight-bearing. Yet, these changes were significant only for the LT in varus alignment, i.e. δ_{var1} vs. δ_{var2} (ThC). Specific anatomic and biomechanical aspects of the knee joint may help explain this finding as the articular surface of the LT is convex, thereby decreasing the area of articulation (Donahue et al., 2002). Consequently, compartmental and regional loading may be borne in a more focal manner, which potentiates the effects of compressive loading in altered alignment. Hence, loading in valgus or varus alignment induced considerably larger relative changes than in neutral alignment, even at moderate loading intensities, and relative changes tended to be relatively homogeneous throughout the entire femoral and tibial cartilage plates. On the sub-regional level, relative changes in ThC revealed distinctly different loading patterns that were reflective of the joint's alignment during compressive loading. In the neutral axis, loading of the medial and lateral femorotibial compartments was mainly borne by the central and,

to a lesser extent, external subregions of the femur and tibia as indicated by the largest relative changes in these subregions. These findings are in line with earlier studies using human knee joints and intraoperative pressure mappings obtained during total knee replacement surgery: Upon axial loading of human knee joint specimens at 1000 N in neutral alignment, Agneskirchner et al. found topographical differences in pressure distribution across the femorotibial compartments with the highest pressurization of the central compartments (Agneskirchner et al., 2007). Earlier pressure mappings on the basis of total knee implants demonstrated similar observations of primary load-bearing through the central areas of the compartment (Werner et al., 2005). Compartmentally different structural adaptations in response to loading are indicated by the fact that the internal subregion of the medial tibia underwent hardly any changes as opposed to the lateral tibia, which might be attributable the slightly increasing valgus alignment with increasing loading intensity that favoured progressively larger involvement of the entire lateral femorotibial compartment, including the inner subregion (Werner et al., 2005).

In varus and valgus alignment, loading-induced cartilage deformation was noted throughout the medial and lateral femorotibial compartments even though relative changes were largest in the central and external subregions of femur and tibia. On the tibial side, the posterior subregions underwent least changes, which may be attributed to the $10°$ flexion position that certainly shifted the contact area to the anterior portion of the femorotibial joint articulation (Ahmed and Burke, 1983), indicating considerably less pressurization of the joint's posterior portion. Correspondingly, on the femoral side, the internal subregions underwent least changes, confirming the more peripheral distribution of mean and peak contact pressures in varus and valgus alignment (Agneskirchner et al., 2007; Takahashi et al., 1997; Werner et al., 2005).

In clinical contexts, meniscus and cartilage pathologies are closely intertwined in OA and beyond (Englund et al., 2009). Consequently, meniscus extrusion is commonly associated with meniscal tears that secondarily compromise hoop tension, malalignment of the joint, and advanced loss of femorotibial cartilage (Crema et al., 2012). Thus, meniscus extrusion is widely considered a predictor of severe structural changes of cartilage and meniscus (Berthiaume et al., 2005; Englund et al., 2011). Weight-bearing increases meniscus extrusion compared to non-weight-bearing (Stehling et al., 2012) and may allow more accurate assessment of load transmission and its failure in OA (Patel et al., 2016). Against this background, we quantitatively evaluated meniscus extrusion in relation to the biomechanical framework conditions as well as histological measures. We found significant increases in the extrusion of the MM and LM in response to compressive loading in neutral alignment and as compared to the unloaded configuration, which is in line with earlier reports (Patel et al., 2016; Stehling et al., 2012). Similarly, loading in varus and valgus alignment brought about equally significant increases in meniscus extrusion, which again confirms the efficient compartmental pressurization thus induced. In *in-vivo* MRI studies, (medial) meniscus extrusion is defined as the protrusion of the meniscus body beyond the tibial plateau by 3 mm or more (Breitenseher et al., 1997). In our study, mean extrusion of the MM (in the unloaded configuration) was determined as 3.7 ± 1.4 mm and increased further with loading. These values are substantially larger than those reported in clinical trials (Patel et al., 2016; Stehling et al., 2012) and may be due to post-mortem degradation of the tissue and the absence of active joint stabilizers, which may have contributed to excessive laxity of the MM and LM and their support structures.

Surprisingly, we did not find significant correlations between relative changes in ThC or ExM and histological or biomechanical reference measures for cartilage or meniscus. Possible explanations involve the overall limited specimen size, potential histological mismatching, largely maintained tissue integrity, and the methodologies used for biomechanical referencing and sequence acquisition. For once, even though specimen size was sufficient to perform sound statistical analyses and derive valid inferences, it was limited to ten specimens. For another,

we harvested cartilage and meniscus along the mid-coronal plane for the sake of standardization. Even though sampled tissue areas were selected to be as representative as possible of the entire compartment, it is not clear how the sampled areas compare to the loaded areas in each of the joint configurations. Also, in light of the heterogeneous molecular and morphologic degenerative processes across the joint (Squires et al., 2003) that involve both the lesion site and the surrounding tissue (Kretzschmar et al., 2019), the sampled tissue areas may not have grasped the compartment's degenerative status in its entirety. Moreover, sampled meniscus and cartilage tissue was grossly intact to only mildly degenerative as indicated by relatively low Mankin and Pauli sum scores. Consequently, the specimens might not have been reflective of the full range of health and disease and our study has thus only defined joint and tissue functionality in intact to largely intact joints of aged donors.

Cartilage degeneration was slightly more severe in the medial as compared to the lateral femorotibial compartment, which is plausible as medial compartment OA is far more common than lateral compartment OA (Wise et al., 2012), most likely because of differences in motion and geometry (Gulati et al., 2009). Surprisingly, the opposite was observed for meniscus degeneration with more severe meniscal degeneration in the lateral femorotibial compartment. As additional patient- and joint-level information on our human knee specimens are lacking, this observation may not be entirely clarified at the moment. Nonetheless, these findings indicate once again the relevance of including alternative reference methodologies for the assessment of tissue status to infer correct conclusions on tissue functionality in health and disease. For biomechanical referencing of cartilage, we used a relatively fast strain rate of 0.15% strain/sec (Nebelung et al., 2017b). As the tissue's response to loading is largely governed by the contribution of fluid pressurization and fibril reinforcement (Li and Herzog, 2004), this relatively high strain rate may have favoured the contribution of fluid over solid intra-tissue changes. Mid-to long-term static compression as induced by our axial compressive loading device is clearly borne by the cartilage extracellular matrix so that slight differences in samples' load-bearing capacities might have been missed. In other words: While the equilibrium behaviour is predominantly governed by the solid matrix and assessed by imaging measures, the instantaneous behaviour is primarily controlled by fluid redistribution and evaluated by the biomechanical reference framework. These discrepancies may explain the lack of correlation between imaging and biomechanical reference measures. Another limitation pertains to the fact that we only used morphometric cartilage and meniscus measures to assess tissue functionality. For more comprehensive joint and tissue functionality assessment, alternative advanced MRI techniques such as T2 or T1ρ mapping or diffusion-weighted imaging sequences may be employed to gain in-depth insights into cartilage (ultra)structure and composition and its changes in response to loading. Furthermore, repeatability of such morphometric measurements was not assessed so that the possibility of permanent alteration of morphology or function secondary to loading cannot be excluded. Even though repeatability assessment is scientifically warranted, it is important to note that any repeat measurement following the successive unloaded (one) and loaded (six) measurements would be subject to two different processes, i.e. continuous post-loading relaxation and progressive post-mortem catabolic degradation. Most likely, these concurrent processes would induce considerable inter-measurement variability and, thus, call into question measurement repeatability in such functional contexts.

Another limitation in our study's setup involves its non-randomized design. Specimen randomization along the three axis configurations, i.e. normal, varus, and valgus, would have substantially reduced statistical unit size and power, and was therefore not performed. Non-randomization, however, comes at the cost of possible bias induced by the sequential testing order of the joint configurations. Persistent reductions in ThC of effectively unloaded compartments, i.e. of the lateral compartment during loading in varus alignment, are the likely result of

ongoing tissue relaxation following loading in neutral alignment. Joint morphology and morphometry are therefore clearly affected by the applied order of testing. Future study designs should therefore use randomization schemes alongside larger specimen sizes to overcome these issues.

Moreover, we only assessed the tissues in equilibrium instead of longitudinally assessing their response to loading and unloading by serial measurements as performed before (Choi et al., 2016; Halonen et al., 2014; Nebelung et al., 2018, 2019a). Accordingly, we can only relate cartilage deformation and meniscus extrusion to static loading and joint configurations, while the study of time-dependent effects was not possible as it requires serial imaging at considerably higher temporal resolution. Future studies to define the imaging features of the cartilage response to loading *in situ* and, possibly, *in vivo* will have to be matched by an adequate biomechanical reference framework. Within this framework, more sophisticated biomechanical methodologies need to be applied that assess the tissue's response to loading beyond preliminary elastic approaches by considering the poro-viscoelastic and depth-dependent tissue responses, possibly accompanied by constitutive material models (Linka et al., 2017, 2019; Thuring et al., 2018).

5. Conclusion

In conclusion, this study is the first to standardize compressive loading *in situ* in different varus and valgus configurations and loading intensities and to assess joint and tissue functionality in the entire joint by a quantitative MRI approach as well as in reference to histological and biomechanical measures. Even though it is well known that axial loading induces changes in cartilage, meniscus, and the entire joint, this study is the first to define response-to-loading patterns of both tissues as surrogate parameters of functionality in the human knee joint in a standardized and controlled experimental setup. Thus, tissue and joint functionality may be defined as a function of loading intensity, joint alignment, histological tissue status, and biomechanical properties. This is another step towards clinical implementation of MRI-based quantitation of joint and tissue functionality and may help to conduct future clinical studies in a more efficient manner. Additionally, further basic research projects may be initiated that deal with alternative MRI techniques (e.g. T2 or T1ρ maps), variable biomechanical loading regimes (e. g. dynamic vs. static loading) or the effects of therapeutic interventions (e.g. cartilage resurfacing or meniscus repair).

Declaration of competing interest

The authors declare that they have no known competing financial interests or personal relationships that could have appeared to influence the work reported in this paper.

CRediT authorship contribution statement

Philipp Schad: Writing - review & editing, Conceptualization, Data

curation, Funding acquisition, Formal analysis, Writing - original draft. **Maximilian Wollenweber:** Conceptualization, Data curation, Funding acquisition, Formal analysis, Writing - original draft. **Johannes Thür-ing:** Conceptualization, Data curation, Funding acquisition, Formal analysis, Writing - original draft. **Justus Schock:** Conceptualization, Data curation, Funding acquisition, Formal analysis, Writing - original draft. **Jörg Eschweiler:** Writing - review & editing, Conceptualization, Data curation, Funding acquisition, Formal analysis, Writing - original draft. **Giulia Palm:** Conceptualization, Data curation, Funding acquisition, Formal analysis, Writing - original draft. **Klaus Radermacher:** Writing - review & editing, Conceptualization, Data curation, Funding acquisition, Formal analysis, Writing - original draft. **Felix Eckstein:** Writing - review & editing, Conceptualization, Data curation, Funding acquisition, Formal analysis, Writing - original draft. **Andreas Prescher:** Conceptualization, Data curation, Funding acquisition, Formal analysis, Writing - original draft. **Christiane Kuhl:** Writing - review & editing, Conceptualization, Data curation, Funding acquisition, Formal analysis, Writing - original draft. **Daniel Truhn:** Writing - review & editing, Conceptualization, Data curation, Funding acquisition, Formal analysis, Writing - original draft. **Sven Nebelung:** Writing - review & editing, Conceptualization, Data curation, Funding acquisition, Formal analysis, Writing - original draft.

Acknowledgements

Appendix A. Supplementary data

Supplementary data to this article can be found online at https://doi.org/10.1016/j.jmbbm.2020.103890.

References

Agneskirchner, J.D., Hurschler, C., Wrann, C.D., Lobenhoffer, P., 2007. The effects of valgus medial opening wedge high tibial osteotomy on articular cartilage pressure of the knee: a biomechanical study. Arthroscopy 23, 852–861.

Ahmed, A.M., Burke, D.L., 1983. In-vitro measurement of static pressure distribution in synovial joints–Part I: tibial surface of the knee. J. Biomech. Eng. 105, 216–225.

Berthiaume, M.J., Raynauld, J.P., Martel-Pelletier, J., Labonte, F., Beaudoin, G., Bloch, D.A., Choquette, D., Haraoui, B., Altman, R.D., Hochberg, M., Meyer, J.M., Cline, G.A., Pelletier, J.P., 2005. Meniscal tear and extrusion are strongly associated with progression of symptomatic knee osteoarthritis as assessed by quantitative magnetic resonance imaging. Ann. Rheum. Dis. 64, 556–563.

Breitenseher, M.J., Trattnig, S., Dobrocky, I., Kukla, C., Nehrer, S., Steiner, E., Imhof, H., 1997. MR imaging of meniscal subluxation in the knee. Acta Radiol. 38, 876–879.

Chan, D.D., Cai, L., Butz, K.D., Trippel, S.B., Nauman, E.A., Neu, C.P., 2016. In vivo articular cartilage deformation: noninvasive quantification of intratissue strain during joint contact in the human knee. Sci. Rep. 6, 19220.

Choi, J.-H., McWalter, E., Datta, S., Mueller, K., Maier, A., Fahrig, R., Levenston, M., Gold, G., 2016. Tibial cartilage creep during weight bearing: in vivo 3D CT assessment. Osteoarthritis Cartilage 24, S104.

Cotofana, S., Eckstein, F., Wirth, W., Souza, R.B., Li, X., Wyman, B., Hellio-Le Graverand, M.P., Link, T., Majumdar, S., 2011. In vivo measures of cartilage deformation: patterns in healthy and osteoarthritic female knees using 3T MR imaging. Eur. Radiol. 21, 1127–1135.

Crema, M.D., Roemer, F.W., Felson, D.T., Englund, M., Wang, K., Jarraya, M., Nevitt, M.C., Marra, M.D., Torner, J.C., Lewis, C.E., 2012. Factors associated with meniscal extrusion in knees with or at risk for osteoarthritis: the Multicenter Osteoarthritis study. Radiology 264, 494–503.

Donahue, T.L., Hull, M.L., Rashid, M.M., Jacobs, C.R., 2002. A finite element model of the human knee joint for the study of tibio-femoral contact. J. Biomech. Eng. 124, 273–280.

Eckstein, F., Guermazi, A., Gold, G., Duryea, J., Le Graverand, M.-P.H., Wirth, W., Miller, D., 2014. Imaging of cartilage and bone: promises and pitfalls in clinical trials of osteoarthritis. Osteoarthritis Cartilage 22, 1516–1532.

Eckstein, F., Lemberger, B., Gratzke, C., Hudelmaier, M., Glaser, C., Englmeier, K.H., Reiser, M., 2005. In vivo cartilage deformation after different types of activity and its dependence on physical training status. Ann. Rheum. Dis. 64, 291–295.

Englund, M., Felson, D.T., Guermazi, A., Roemer, F.W., Wang, K., Crema, M.D., Lynch, J.A., Sharma, L., Segal, N.A., Lewis, C.E., Nevitt, M.C., 2011. Risk factors for medial meniscal pathology on knee MRI in older US adults: a multicentre prospective cohort study. Ann. Rheum. Dis. 70, 1733–1739.

Englund, M., Guermazi, A., Lohmander, S.L., 2009. The role of the meniscus in knee osteoarthritis: a cause or consequence? Radiol. Clin. 47, 703–712.

Fischenich, K.M., Lewis, J., Kindsfater, K.A., Bailey, T.S., Haut Donahue, T.L., 2015. Effects of degeneration on the compressive and tensile properties of human meniscus. J. Biomech. 48, 1407–1411.

Gold, G.E., Chen, C.A., Koo, S., Hargreaves, B.A., Bangerter, N.K., 2009. Recent advances in MRI of articular cartilage. Am. J. Roentgenol. 193, 628–638.

Gulati, A., Chau, R., Beard, D.J., Price, A.J., Gill, H.S., Murray, D.W., 2009. Localization of the full-thickness cartilage lesions in medial and lateral unicompartmental knee osteoarthritis. J. Orthop. Res. 27, 1339–1346.

Halonen, K., Mononen, M., Jurvelin, J., Töyräs, J., Salo, J., Korhonen, R., 2014. Deformation of articular cartilage during static loading of a knee joint–experimental and finite element analysis. J. Biomech. 47, 2467–2474.

Herberhold, C., Faber, S., Stammberger, T., Steinlechner, M., Putz, R., Englmeier, K.H., Reiser, M., Eckstein, F., 1999. In situ measurement of articular cartilage deformation in intact femoropatellar joints under static loading. J. Biomech. 32, 1287–1295.

Jandaghi, A.B., Mardani-Kivi, M., Mirbolook, A., Emami-Meybodi, M.K., Mohammadzadeh, S., Farahmand, M., 2016. Comparison of indirect MR arthrography with conventional MRI in the diagnosis of knee pathologies in patients with knee pain. Trauma Mon. 21.

Jerban, S., Chang, E.Y., Du, J., 2020. Magnetic resonance imaging (MRI) studies of knee joint under mechanical loading. Magn. Reson. Imag. 65, 27–36.

Kellgren, J.H., Lawrence, J.S., 1957. Radiological assessment of osteo-arthrosis. Ann. Rheum. Dis. 16, 494–502.

Kleemann, R.U., Krocker, D., Cedraro, A., Tuischer, J., Duda, G.N., 2005. Altered cartilage mechanics and histology in knee osteoarthritis: relation to clinical assessment (ICRS Grade). Osteoarthritis Cartilage 13, 958–963.

Kretzschmar, M., Nevitt, M.C., Schwaiger, B.J., Joseph, G.B., McCulloch, C.E., Link, T.M., 2019. Spatial distribution and temporal progression of T2 relaxation time values in knee cartilage prior to the onset of cartilage lesions - data from the Osteoarthritis Initiative (OAI). Osteoarthritis Cartilage 27, 737–745.

Li, L.P., Herzog, W., 2004. Strain-rate dependence of cartilage stiffness in unconfined compression: the role of fibril reinforcement versus tissue volume change in fluid pressurization. J. Biomech. 37, 375–382.

Linka, K., Itskov, M., Truhn, D., Nebelung, S., Thuring, J., 2017. T2 MR imaging vs. computational modeling of human articular cartilage tissue functionality. J. Mech. Behav. Biomed. Mater. 74, 477–487.

Linka, K., Schafer, A., Hillgartner, M., Itskov, M., Knobe, M., Kuhl, C., Hitpass, L., Truhn, D., Thuering, J., Nebelung, S., 2019. Towards patient-specific computational modelling of articular cartilage on the basis of advanced multiparametric MRI techniques. Sci. Rep. 9, 7172.

Mankin, H.J., Dorfman, H., Lippiello, L., Zarins, A., 1971. Biochemical and metabolic abnormalities in articular cartilage from osteo-arthritic human hips. II. Correlation of morphology with biochemical and metabolic data. J. Bone Joint Surg. Am. 53, 523–537.

Nebelung, S., Dotsch, L., Shah, D., Abrar, D.B., Linka, K., Knobe, M., Sewerin, P., Thuring, J., Kuhl, C., Truhn, D., 2020. Functional MRI mapping of human meniscus functionality and its relation to degeneration. Sci. Rep. 10, 2499.

Nebelung, S., Post, M., Knobe, M., Shah, D., Schleich, C., Hitpass, L., Kuhl, C., Thuring, J., Truhn, D., 2019a. Human articular cartilage mechanosensitivity is related to histological degeneration - a functional MRI study. Osteoarthritis Cartilage 27, 1711–1720.

Nebelung, S., Post, M., Knobe, M., Tingart, M., Emans, P., Thuring, J., Kuhl, C., Truhn, D., 2019b. Detection of early-stage degeneration in human articular cartilage by multiparametric MR imaging mapping of tissue functionality. Sci. Rep. 9, 5895.

Nebelung, S., Post, M., Raith, S., Fischer, H., Knobe, M., Braun, B., Prescher, A., Tingart, M., Thuring, J., Bruners, P., Jahr, H., Kuhl, C., Truhn, D., 2017a. Functional in situ assessment of human articular cartilage using MRI: a whole-knee joint loading device. Biomech. Model. Mechanobiol. 16, 1971–1986.

Nebelung, S., Sondern, B., Jahr, H., Tingart, M., Knobe, M., Thuring, J., Kuhl, C., Truhn, D., 2018. Non-invasive T1rho mapping of the human cartilage response to loading and unloading. Osteoarthritis Cartilage 26, 236–244.

Nebelung, S., Sondern, B., Oehrl, S., Tingart, M., Rath, B., Pufe, T., Raith, S., Fischer, H., Kuhl, C., Jahr, H., Truhn, D., 2017b. Functional MR imaging mapping of human articular cartilage response to loading. Radiology 282, 464–474.

Palmer, A.J., Brown, C.P., McNally, E.G., Price, A.J., Tracey, I., Jezzard, P., Carr, A.J., Glyn-Jones, S., 2013. Non-invasive imaging of cartilage in early osteoarthritis. Bone Joint J. 95-B, 738–746.

Patel, R., Eltgroth, M., Souza, R., Zhang, C.A., Majumdar, S., Link, T.M., Motamedi, D., 2016. Loaded versus unloaded magnetic resonance imaging (MRI) of the knee: effect on meniscus extrusion in healthy volunteers and patients with osteoarthritis. Eur. J. Radiol. Open. 3, 100–107.

Pauli, C., Grogan, S.P., Patil, S., Otsuki, S., Hasegawa, A., Koziol, J., Lotz, M.K., D'Lima, D.D., 2011. Macroscopic and histopathologic analysis of human knee menisci in aging and osteoarthritis. Osteoarthritis Cartilage 19, 1132–1141.

Phelan, N., Rowland, P., Galvin, R., O'Byrne, J.M., 2016. A systematic review and meta-analysis of the diagnostic accuracy of MRI for suspected ACL and meniscal tears of the knee. Knee Surg. Sports Traumatol. Arthrosc. 24, 1525–1539.

Roemer, F.W., Crema, M.D., Trattnig, S., Guermazi, A., 2011. Advances in imaging of osteoarthritis and cartilage. Radiology 260, 332–354.

Roemer, F.W., Kwoh, C.K., Hayashi, D., Felson, D.T., Guermazi, A., 2018. The role of radiography and MRI for eligibility assessment in DMOAD trials of knee OA. Nat. Rev. Rheumatol. 14, 372–380.

Rogers, A.D., Payne, J.E., Joseph, S.Y., 2013. Cartilage imaging: a review of current concepts and emerging technologies. Semin. Roentgenol. 148–157.

Saarakkala, S., Julkunen, P., Kiviranta, P., Makitalo, J., Jurvelin, J.S., Korhonen, R.K., 2010. Depth-wise progression of osteoarthritis in human articular cartilage: investigation of composition, structure and biomechanics. Osteoarthritis Cartilage 18, 73–81.

Shin, C.S., Souza, R.B., Kumar, D., Link, T.M., Wyman, B.T., Majumdar, S., 2011. In vivo tibiofemoral cartilage-to-cartilage contact area of females with medial osteoarthritis under acute loading using MRI. J. Magn. Reson. Imag. : JMRI 34, 1405–1413.

Souza, R.B., Kumar, D., Calixto, N., Singh, J., Schooler, J., Subburaj, K., Li, X., Link, T.M., Majumdar, S., 2014. Response of knee cartilage T1rho and T2 relaxation times to in vivo mechanical loading in individuals with and without knee osteoarthritis. Osteoarthritis Cartilage 22, 1367–1376.

Souza, R.B., Stehling, C., Wyman, B.T., Hellio Le Graverand, M.P., Li, X., Link, T.M., Majumdar, S., 2010. The effects of acute loading on T1rho and T2 relaxation times of tibiofemoral articular cartilage. Osteoarthritis Cartilage 18, 1557–1563.

Squires, G.R., Okouneff, S., Ionescu, M., Poole, A.R., 2003. The pathobiology of focal lesion development in aging human articular cartilage and molecular matrix changes characteristic of osteoarthritis. Arthritis Rheum. 48, 1261–1270.

Stehling, C., Souza, R.B., Hellio Le Graverand, M.P., Wyman, B.T., Li, X., Majumdar, S., Link, T.M., 2012. Loading of the knee during 3.0T MRI is associated with significantly increased medial meniscus extrusion in mild and moderate osteoarthritis. Eur. J. Radiol. 81, 1839–1845.

Subburaj, K., Souza, R.B., Stehling, C., Wyman, B.T., Le Graverand-Gastineau, M.P., Link, T.M., Li, X., Majumdar, S., 2012. Association of MR relaxation and cartilage deformation in knee osteoarthritis. J. Orthop. Res. 30, 919–926.

Suero, E.M., Hawi, N., Westphal, R., Sabbagh, Y., Citak, M., Wahl, F.M., Krettek, C., Liodakis, E., 2017. The effect of distal tibial rotation during high tibial osteotomy on the contact pressures in the knee and ankle joints. Knee Surg. Sports Traumatol. Arthrosc. 25, 299–305.

Suero, E.M., Sabbagh, Y., Westphal, R., Hawi, N., Citak, M., Wahl, F.M., Krettek, C., Liodakis, E., 2015. Effect of medial opening wedge high tibial osteotomy on intraarticular knee and ankle contact pressures. J. Orthop. Res. 33, 598–604.

Takahashi, T., Wada, Y., Yamamoto, H., 1997. Soft-tissue balancing with pressure distribution during total knee arthroplasty. J. Bone Joint Surg. 79, 235–239. British volume.

Thuring, J., Linka, K., Itskov, M., Knobe, M., Hitpass, L., Kuhl, C., Truhn, D., Nebelung, S., 2018. Multiparametric MRI and computational modelling in the assessment of human articular cartilage properties: a comprehensive approach. BioMed Res. Int. 2018, 9460456.

Truhn, D., Brill, N., Braun, B., Merhof, D., Kuhl, C., Knobe, M., Thuering, J., Nebelung, S., 2020. A multi-purpose force-controlled loading device for cartilage and meniscus functionality assessment using advanced MRI techniques. J. Mech. Behav. Biomed. Mater. 101, 103428.

Truhn, D., Sondern, B., Oehrl, S., Tingart, M., Knobe, M., Merhof, D., Kuhl, C., Thuring, J., Nebelung, S., 2019. Differentiation of human cartilage degeneration by functional MRI mapping-an ex vivo study. Eur. Radiol. 29, 6671–6681.

Walpole, S.C., Prieto-Merino, D., Edwards, P., Cleland, J., Stevens, G., Roberts, I., 2012. The weight of nations: an estimation of adult human biomass. BMC Publ. Health 12, 439.

Wang, H., Koff, M.F., Potter, H.G., Warren, R.F., Rodeo, S.A., Maher, S.A., 2015. An MRI-compatible loading device to assess knee joint cartilage deformation: effect of preloading and inter-test repeatability. J. Biomech. 48, 2934–2940.

Werner, F.W., Ayers, D.C., Maletsky, L.P., Rullkoetter, P.J., 2005. The effect of valgus/varus malalignment on load distribution in total knee replacements. J. Biomech. 38, 349–355.

Winby, C.R., Lloyd, D.G., Besier, T.F., Kirk, T.B., 2009. Muscle and external load contribution to knee joint contact loads during normal gait. J. Biomech. 42, 2294–2300.

Wirth, W., Eckstein, F., 2008. A technique for regional analysis of femorotibial cartilage thickness based on quantitative magnetic resonance imaging. IEEE Trans. Med. Imag. 27, 737–744.

Wise, B.L., Niu, J., Yang, M., Lane, N.E., Harvey, W., Felson, D.T., Hietpas, J., Nevitt, M., Sharma, L., Torner, J., 2012. Patterns of compartment involvement in tibiofemoral osteoarthritis in men and women and in whites and African Americans. Arthritis Care Res. 64, 847–852.

Zevenbergen, L., Gsell, W., Chan, D.D., Vander Sloten, J., Himmelreich, U., Neu, C.P., Jonkers, I., 2018. Functional Assessment of Strains Around a Full-Thickness and Critical Sized Articular Cartilage Defect under Compressive Loading Using MRI. Osteoarthritis Cartilage.